

# Experimental Investigation of E-beam Effect on Electric Field Distribution in Cross-Linked Polyethylene/ZnO Nanocomposites for Medium-Voltage Cables Simulated Using COMSOL Multiphysics

A. I. Sharshir (✉ [a.shr88@yahoo.com](mailto:a.shr88@yahoo.com))

<https://orcid.org/0000-0002-5602-4074>

S. A. Fayek

Amal. F. Abd El-Gawad

M. A. Farahat

M. I. Ismail

Mohamed Mohamady Ghobashy

---

## Research Article

**Keywords:** cross-linked polyethylene cable, electron beam irradiation, COMSOL Multiphysics, zinc oxide NPs

**Posted Date:** February 15th, 2022

**DOI:** <https://doi.org/10.21203/rs.3.rs-1338067/v1>

**License:**   This work is licensed under a Creative Commons Attribution 4.0 International License.

[Read Full License](#)

---

# Abstract

This study investigated the electric field distribution of underground cable insulation in cross-linked polyethylene/zinc oxide (XLPE/ZnO) NPs for medium-voltage (MV) cables. The ZnO NPs that were obtained by three methods of preparation were classified using transmission electron microscopy (TEM). The obtained ZnO NPs were semi-spheres with sizes of 35–55 nm on TEM images. XLPE/ZnO films with various ZnO NP weight contents (i.e., 0%, 1%, 3%, and 5%) were exposed to varied dosages of 3-MeV electron beam (i.e., 0 kGy, 15 kGy, 20 kGy, and 25 kGy). The optimum film XLPE/5-ZnO, which has ZnO NP content (5 wt%), irradiated at 25 kGy, according to alternating current (AC)/DC conductivity (AC:  $1 \times 10^{-4}$  S/m; DC:  $12.44 \times 10^{-2}$  S/m) in minimum relative permittivity (2.24), was obtained. COMSOL Multiphysics was used to simulate the electric field distribution within an MV cable of 25-kGy XLPE/5-ZnO insulation. The maximum uniform electric field was found in the middle of the 25-kGy XLPE/5-ZnO film sample, rather than at the top or bottom, which might be attributed to the significantly low relative permittivity of the new 25-kGy XLPE/5-ZnO film cable.

## 1. Introduction

Because of their outstanding electrical, thermal, mechanical, and chemical characteristics, nanofillers, such as zinc oxide (ZnO), have received so much interest in further strengthening composites. The addition of ZnO to a polymer matrix can improve load transmission and composite strength. As a result, by incorporating nanofillers into current polymer systems, composite performance and application range can be enhanced [1]. Because of their intrinsic characteristics, nanofillers are particularly essential in developing polymer nanocomposites. Some NPs (e.g., ZnO) have outstanding stability, a high refractive index, hydrophilicity, ultraviolet (UV) resistance, great transparency to visible light, nontoxicity, strong photocatalytic activity, and low cost. ZnO may be made into various nanostructures, including nanorods, nanowires, spherical NPs, and tetrapods, and is a multifunctional n-type (II–V) semiconductor with a large binding energy (60 meV), excellent UV absorbance, and a broad band gap (3.4 eV) [2]. Because ZnO is nontoxic and environmentally benign, it may be used in bio-applications and is a low cost substance found in conductive glass, white paint, and commercialized sunscreens [3]. ZnO NPs (NPs) have unique properties allowing them to exist in either an anti-electrostatic or conductive state. In the literature, the electrical [4], magnetic [5], chemical [6], and optical [7] properties of ZnO NPs are remarkable. It has been used in catalysis and semiconductor manufacturing.

The high exciton-binding energy of ZnO would allow for excitonic transitions even at room temperature, which could mean high radiative recombination efficiency for spontaneous emission and a lower threshold voltage for laser emission. The lack of a center of symmetry in wurtzite, combined with a large electromechanical coupling, results in strong piezoelectric and pyroelectric properties and, hence, the use of ZnO in mechanical actuators and piezoelectric sensors [8, 9]. ZnO is a potential candidate for optoelectronic applications in the short wavelength range (i.e., green, blue, and UV), information storage, and sensors as it exhibits properties similar to those of GaN [10–12]. ZnO NPs are promising candidates for various applications, such as nanogenerators [13], gas sensors [14], biosensors [15], solar cells [16],

varistors [17], photodetectors [18], photocatalysts [19], piezoelectric, transducers and light-emitting diodes, various optoelectronic devices, biomedical applications, plant science, and wastewater treatment [20–22]. From a literature review, it was found that various approaches for preparing ZnO nanopowders have been developed, namely, sol-gel, microemulsion, thermal decomposition of organic precursor, spray pyrolysis, electrodeposition, ultrasonic, microwave-assisted techniques, chemical vapor deposition, and hydrothermal and precipitation methods [23–32].

Electron beam (EB) irradiation technique has lately become a sophisticated approach for improving material physical properties like thermal stability, structural, conductivity and mechanical. When EB energy interacts with polymer material, it promotes molecular structural changes like atom displacement, carbonization, ionization, and the generation of free radicals, which aid in chain scission and cross-linking processes. As a result, polymer matrices has become a important research topic in science, especially in industrial applications such cable, wire, electrical devices, marine, and medical. Radiation can only alter the polymer's chemical makeup; however, it can also enhance the presence of trapped charges or produce matrix defects [33]. Physical characteristics are directly affected by this structural change in the irradiated polymer electrolyte; in this case, dielectric permittivity and electrical conductivity improved as the dosage was raised. The above modifications are influenced by the physics and chemistry of the absorbed products, as well as the selected radiation energy and dose as a result of cross-linking or chain scission. The existence of trapping charge within the material was affected by the induced radiation, which increased the transport property. It's also been discovered that altering a polymer's functional group alters the physical characteristics of polymer films. Changes in electrical, dielectric, and thermal characteristics occur as a result of irradiated polymers can be attributed to these changes [34, 35]. In other words, irradiated polymers can be converted from insulators to materials with good electrical conductivity, which is a good sign since these materials can be used in various electronic applications.

Sharshir et al. [36] have used a melt mixer to prepare cross-linked polyethylene (XLPE) cables composited with copper NPs (CuNPs). Different NP ratios were used to make the XLPE/Cu nanocomposites (i.e., 0, 1, 3, and 5 wt%) at different EB irradiation doses of 0, 15, 20, and 25 kGy. In a frequency range of 50–1.5 MHz, the relative permittivity ( $\epsilon_r$ ), dielectric constant ( $\epsilon'$ ), dielectric loss factor ( $\epsilon''$ ), and conductivity ( $\tan$ ) were calculated. The improvement in the electric field uniform occurs in the middle of the 25-kGy XLPE/5-ZnO film cable that has a CuNP content of 5 wt% and irradiated at 25 kGy.

Kim et al. [37] have highlighted in a recent study that the undertaken modifications in the chemical and physical structures of XLPE insulation behavior, under thermal aging, lead to many changes in the dielectric characteristics of XLPE. The mechanical properties of XLPE decreased. From another viewpoint, the leakage current can be considered an important indicator of high-voltage insulation degradation. Moreover, the leakage current can flow through the surface and/or bulk of the materials, and this current can have a solid relation with the aging process. Lei, Weiqun, et al. [38] have examined the preparation of XLPE/silicon dioxide (SiO<sub>2</sub>) nanocomposites, which used DC currents. The strength of the nanobreakdown composite was considerably greater than that of the unfilled XLPE in the DC phase test.

The difference between the typical lives of the nanocomposite and its empty base polymer dropped when the applied field was reduced, and the lifetimes were relatively similar when the applied field was 130 kV/mm, according to endurance tests.

Here, XLPE/ZnO nanocomposites were thoroughly investigated according to the impact of various contents of ZnO on XLPE polymers, including simulating the electric field distribution. The XLPE/ZnO nanocomposites irradiated with EB were simulated using the COMSOL Multiphysics program. The first part of this study is about the preparation and characterization of ZnO NPs. The second part explains the simulation steps and shows how electric field strength propagates in ZnO NPs filled with XLPE medium-voltage (MV) cables. When ZnO NPs were filled into XLPE, they increased conductivity and decreased permittivity, resulting in a uniform electric field arising from the current flow via MV cables.

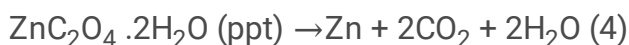
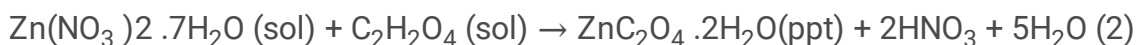
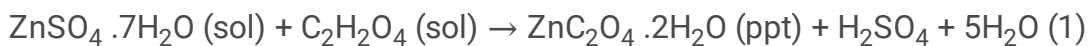
## 2. Material And Experimental Section

XLPE pellets were supplied by El Sewedy, Giza Cables Company, Egypt. They were used for XLPE MV cable manufacture (33 KV). Zinc acetate dihydrate ( $\text{Zn}(\text{CH}_3\text{CO}_2)_2$ ), oxalic acid (OX) ( $\text{C}_2\text{H}_2\text{O}_4$ ), and ammonium hydroxide ( $\text{NH}_4\text{OH}$ ) were supplied by Sigma-Aldrich (Missouri, USA).

The typical procedures for preparing ZnO NPs using three methods are outlined as follows:

### 2.1. OX method ((ZnO)OX)

$\text{Zn}(\text{CH}_3\text{CO}_2)_2 \cdot 2\text{H}_2\text{O}$  (1M) and  $\text{C}_2\text{H}_2\text{O}_4$  (1M) were separately dissolved in distilled water to form homogenous solutions of (A) and (B), respectively. (A) and (B) were mixed thoroughly under vigorous stirring conditions for 30 min and under sonication at ambient temperature up to the formation of white precipitate of zinc oxalate dehydrate ( $\text{ZnC}_2\text{O}_4 \cdot 2\text{H}_2\text{O}$ ). The precipitate was then washed several times with distilled water and dried in an oven at  $100^\circ\text{C}$  for 2 h to remove water, followed by heat treatment at  $800^\circ\text{C}$  for 2 h to obtain a fine powder of Zn metal. The samples were structurally and morphologically examined using an X-ray powder diffractometer. The reactions for the formation of zinc oxalate dihydrate from the salts were as follows:



### 2.2. Metal displacement reaction (MDR) method ((ZnO)MDR)

An appropriate weight of aluminum (Al) powder was added to the  $\text{Zn}(\text{CH}_3\text{CO}_2)_2 \cdot 2\text{H}_2\text{O}$  solution. The reaction was stood for 24 h under sonication conditions. The color changes in the  $\text{Zn}(\text{CH}_3\text{CO}_2)_2 \cdot 2\text{H}_2\text{O}$  solution indicated the beginning of Zn metal formation.

### 2.3. Metal oxide precipitation (MOP) method ((ZnO)MOP)

$\text{NH}_4\text{OH}$  was added drop by drop to the  $\text{Zn}(\text{CH}_3\text{CO}_2)_2 \cdot 2\text{H}_2\text{O}$  solution until it provides gelatinous weight precipitates of zinc hydroxide. The precipitate was washed several times with distilled water and dried in an oven at  $100^\circ\text{C}$  for 2 h to remove water, followed by heat treatment at  $800^\circ\text{C}$  for 2 h to obtain a fine powder of Zn metal.

### 2.4. AC and DC conductivity of different contents of ZnO NP-filled XLPE.

The I–V characteristics (ZnO NPs/XLPE) of the sample were measured at room temperature. We used Keithley source measure units (model 2635A) to measure the I–V characteristics, which were regulated by specially designed ACS Basic Software (Keithley). The LCR bridge model Hioki 3532 was used to measure the sample (ZnO NPs/XLPE) impedance  $Z$  and the phase angle between the applied AC voltage and the resulting current in the sample (ZnO NPs/XLPE) for AC conductivity measurement  $\sigma_{\text{AC}}(\omega)$ . The frequency ranged from 50 Hz to 1.5 MHz (0.05:1500 KHz).

The variation in AC conductivity with a frequency at ambient temperature was examined on the  $\ln$ – $\ln$  scale. The variance of AC and DC with a frequency ranging from 50 Hz to 1.5 MHz was studied for the investigated compositions (all of which had the same thickness (5 mm)). At various ZnO NP concentrations, the obtained results were plotted as  $\ln \sigma_{\text{AC}}(w)$  versus  $\ln w$ .

The sample impedance ( $Z$ ), sample capacitance ( $C_p$ ), and loss tangent ( $\text{Tan}\delta$ ) were directly measured using a programmable automatic 3532 LCR meter. The resistance  $R$  was parallel to all values of  $C_p$ , which was taken from the bridge's screen. The equation used to calculate the total conductivity  $\sigma_t(w)$  was as follows:

$$\sigma_t(w) = L/ZA,$$

where  $L$  is the distance between the two electrodes (the sample thickness),  $Z$  is the impedance of the sample, and  $A$  is the cross-sectional area of the sample. Using the relation, the AC conductivity ( $\sigma_{\text{AC}}(w)$ ) is calculated as follows:

$$\sigma_{\text{AC}}(w) = \sigma_t(w) - \sigma_{\text{DC}}(w)$$

where  $\sigma_{\text{DC}}(w)$  is termed as the DC conductivity.

### 2.5. Preparation of (XLPE/ZnO) nanocomposites

Before mixed process XLPE pellets and ZnO nanoparticles powder were dried overnight at 70°C in an oven remove excess moisture. The XLPE pellets were mixed with weight contents of ZnO nanoparticles (0, 1, 3 and 5) wt% using a mechanical mixer. The mixing process was carried out at temperature of 170°C under a rotor speed of 120 rpm and the mixing time is 5 min. then the meld (XLPE/ZnO) samples were molded using in the rectangle mold which was heated to 190°C and were held for 5 minutes under a mechanical press to be fully melted. The tableting machine pressure was kept at 10 MPa and the mold temperature was decrease to 50°C for 5 minutes. The tableting machine pressure and the mold temperature was decrease to the ambient pressure and temperature, respectively. The mixing and molding process was the same procedure as the blank sample was prepared. Then all samples are exposed to different electron beam irradiation doses of (0, 15, 20 and 25 kGy).

## **2.6. Composite irradiation.**

A linear particle accelerator (Vivi rad company, France) of 3.0 MeV electron flux with 30 mA at rated current and conveyer speed 16 m/min was used for the irradiation of the samples. The dimension of source electron beam accelerator was (80×70) cm. The minimum dose was 3kGy. The dose rate depended on conveyer speed and current. The films were irradiated at ambient temperature by accelerated electrons until the absorbed doses of 15 and 25 kGy were reached.

## **2.7. Simulation Procedure of electric field distribution.**

The electric field distribution was studied starting from the copper core to the outer semiconductor layer of the cable. The cable layers were subjected to a constant  $2U_0 = 24$  kV 50 Hz AC power supply (where  $U_0$  is the cable's rated line to neutral voltage). The electric fields effects were then investigated using COMSOL Multiphysics. As a compression sample in this study, the XLPE marked cable used was a single-core 22 kV shielded underground cable. The copper conductor with a 4.165 mm radius, inner semiconductor of 4.95 mm, XLPE insulation of 10.45 mm and outer semiconductor of 11.25 mm are useful layers used in the analysis. All radii have been estimated from the middle of the copper conductor.

## **2.8. Characterization of zinc oxide nanoparticles**

Ultraviolet-visible spectrophotometer (Ultraviolet-3600, Shimadzu) was utilized to monitor the characterization of the synthesised ZnO nanoparticles at a scanning range of 200-700 nm, and autoclaved gum utilized as a blank. The Fourier-transform infrared spectroscopy (FTIR/ATR) is a technique used to obtain an infrared spectrum of a solid samples of ZnO nanoparticles. The powder-XRD technique was utilized by (XRD-7000 Shimadzu), Germany. The process for crystalline analysis of the ZnONPs with Cuka radiation ( $\lambda = 1.5418$  Å) Shimadzu. The Transmission Electron Microscopes (TEM) has used to determent the size and morphology of the prepared ZnONPs. The sample grid was primed for TEM calculation by inserting a drop in aqueous ZnONPs dispersion in acetone solvent on the carbon-coated copper grid, and then evaporating the water spontaneously overnight under atmospheric conditions.

## **3. Results And Discussion**

### 3.1. The physicochemical properties of ZnO NPs prepared using three preparation methods

X-ray diffraction (XRD) was used to differentiate between ZnO nanoparticles obtained using the three methods and the presence of zinc dioxide ( $\text{ZnO}_2$ ) NPs. Figure 1a shows the XRD patterns of ZnO NPs obtained using the (ZnO)OX, (ZnO)MDR, and (ZnO)MOP methods, which displayed peaks of both ZnO and  $\text{ZnO}_2$  NPs on XRD according to the International Center for Diffraction Data (ICDD) (89–1,397 and 77–2,414, respectively). All ZnO NP samples were in the crystalline form (Figure 1a). For the (ZnO)OX sample, three distinct XRD peaks were found located at  $2\theta = 31.68^\circ$ ,  $34.34^\circ$ , and  $36.17^\circ$ , which corresponded to the lattice patterns of 100, 002, and 101 face-centered cubic of pure ZnO NPs, respectively, and six intensity peaks were displayed located at  $2\theta = 47.47^\circ$ ,  $56.53^\circ$ ,  $62.79^\circ$ ,  $66.27^\circ$ ,  $67.88^\circ$ , and  $69.02^\circ$ , which corresponded to  $\text{ZnO}_2$  NPs. For the (ZnO)MDR sample, 10 intensity peaks were found located at  $2\theta = 31.65^\circ$ ,  $34.28^\circ$ ,  $36.13^\circ$ ,  $47.46^\circ$ ,  $56.52^\circ$ ,  $62.76^\circ$ ,  $66.27^\circ$ ,  $67.86^\circ$ ,  $69.01^\circ$ , and  $72.17^\circ$ , which corresponded to ZnO NPs. These peaks fully fit File ICDD No. 89-1397, which confirmed the creation of pure crystal ZnO NPs. The two weak-intensity peaks located at  $2\theta = 78.09^\circ$  and  $81.47^\circ$  corresponded to  $\text{ZnO}_2$  NPs according to File ICDD No. 77-2414. For the (ZnO)MOP sample, the XRD curve showed seven intensity peaks located at  $2\theta = 31.83^\circ$ ,  $34.56^\circ$ ,  $36.34^\circ$ ,  $47.66^\circ$ ,  $56.65^\circ$ ,  $68.04^\circ$ , and  $69.14^\circ$ , which corresponded to ZnO NPs according to File ICDD No. 89-1397. The two weak-intensity peaks located at  $2\theta = 63.02^\circ$  and  $66.44^\circ$  corresponded to  $\text{ZnO}_2$  NPs according to File ICDD No. 77-2414. The percentage of NP structures in ZnO was verified using XRD pattern analysis. Consistent with the XRD data, such as the intensity of peaks, Table 1 shows that ZnO NPs were the most abundant phase in the (ZnO)OX sample (100%), followed by (ZnO)MDR and (ZnO)MOP with the content of 97.97% and 89.63%, respectively, whereas  $\text{ZnO}_2$  was the most abundant phase in the (ZnO)MDR sample (2.03%), and  $\text{ZnO}_2$  was the most abundant phase in the (ZnO)MOP sample (10.37%). These data confirm that (ZnO)OX is an abbreviated technique for preparing pure ZnO NPs.

Figure 1b represents the Fourier transform infrared spectroscopy (FTIR) spectra of ZnO NPs obtained from three preparation methods, such as (ZnO)OX, (ZnO)MDR, and (ZnO)MOP. These FTIR spectra revealed a peak located at  $\sim 600 \text{ cm}^{-1}$  that attributed to ZnO bonds, and the FTIR peak located at  $\sim 870 \text{ cm}^{-1}$  was attributed to Zn-OH bonds [39]. It is clear from Figure 1b that Zn-O bonds exist in all ZnO NP samples, and Zn-OH bonds are present in the ZnO sample only.

Figure 1c represents the transmission electron microscopy (TEM) image of ZnO NPs prepared using the OX method ((ZnO)OX). These ZnO NPs obtained using the (ZnO)OX method were almost spherical in shape, and their morphology was the same with a mean size of  $35 \text{ nm} \pm 10 \text{ nm}$  because the creation of ZnO NPs was quick without agglomeration observation (Figure 1c).

**Table 1** X-ray diffraction analysis of the zinc oxide (ZnO) nanoparticle (NP) samples prepared using three methods—(ZnO)OX, (ZnO)MDR, and (ZnO)MOP—showing the variation in ZnO NP content according to the preparation method used.

Sample	ZnO%	ZnO <sub>2</sub> %
(ZnO)OX	100	0
(ZnO)MDR	97.97	2.03
(ZnO)MOP	89.63	10.37

The three band gaps of ZnO NPs (i.e., (ZnO)OX, (ZnO)MDR, and (ZnO)MOP) are shown in Figure 2. The band gaps ranged from 3.12 eV to 3.3 eV since the values depended on several factors, such as the particle size and purity of the ZnO produced. Table 2 shows how to determine the band gap, for example, by extending the straight part to the energy axis at  $(\alpha)^2 = 0$ . When it can be observed, the band gap increased as the oxidation of ZnO occurs [40].

Table 2  
Optical band gap of zinc oxide nanoparticles obtained using different preparation methods.

Sample	(ZnO)OX	(ZnO)MDR	(ZnO)MOP
Optical band gap ( $E_g$ )	3.12	3.2	3.3

### 3.2. I–V characteristics curve of ZnO NPs prepared using the three methods

The I–V characteristic curves of the ZnO NPs prepared using three methods—(ZnO)OX, (ZnO)MDR, and (ZnO)MOP—are shown in Figure 3. In the I–V curves, ohmic behavior was observed in ZnO NPs prepared using the three methods. In the first and third quarters, the I–V characteristics were nearly symmetrical, confirming the same resistance. Table 3 shows that the resistance of ZnO NPs prepared using the three methods is equal to 22.22  $\Omega$ , 33.33  $\Omega$ , and 50  $\Omega$ , respectively. The resistance of ZnO NPs prepared using the ZnO1 method was lower than that of ZnO NPs prepared using other methods (i.e., ZnO2 and ZnO3). The conductivity of ZnO NPs was measured using the three preparation methods, which equaled 3.58, 2.39, and 1.59 S/m, respectively (Table 3). The conductivity of ZnO NPs prepared using the (ZnO)OX method was higher than that of ZnO NPs prepared using other methods (i.e., (ZnO)MDR and (ZnO)MOP) because of the increased conductivity with decreasing oxidation. The ZnO NPs prepared using the OX method will be used in the electric field distribution study of the XLPE/ZnO nanocomposite system based on the aforementioned results.

Table 3  
The resistance and conductivity of zinc oxide nanoparticles obtained using the three preparation methods.

Sample	Resistance ( $\Omega$ )	Conductivity (S/m)
(ZnO)OX	22.22	3.58
(ZnO)MDR	33.33	2.39
(ZnO)MOP	50	1.59

### 3.3. The effect of EB irradiation doses on the I–V characteristic curve of XLPE/ZnO-5 nanocomposites.

The I–V characteristic curves of XLPE/ZnO irradiated with four doses of EB at 0, 15, 20, and 25 kGy at 5% ZnO-OX concentration are shown in Figure 4. In the I–V curves, ohmic behavior was observed in XLPE/5-ZnO. In the first and third quarters, the I–V characteristics were nearly symmetrical, confirming the same resistance. Table 4 shows that the resistance of XLPE/5-ZnO irradiated at 0, 15, 20, and 25 kGy was equal to  $2.67 \times 10^3 \Omega$ ,  $1.60 \times 10^3 \Omega$ ,  $1.45 \times 10^3 \Omega$ , and  $0.64 \times 10^3 \Omega$ , respectively. The resistance of XLPE/5-ZnO irradiated at 25 kGy was lower than that of XLPE/5-ZnO irradiated at 0 kGy, 15 kGy, and 20 kGy). Then, the conductivity of XLPE/5-ZnO irradiated at 0, 15, 20, and 25 kGy) was  $2.98 \times 10^{-2}$  S/m,  $4.97 \times 10^{-2}$  S/m,  $5.49 \times 10^{-2}$  S/m, and  $12.44 \times 10^{-2}$  S/m, respectively. The resistance of XLPE/5-ZnO at 25 kGy was the lowest, whereas the conductivity of ZnO NP-filled XLPE at 25 kGy and concentration of 5% ZnO-OX were the greatest, according to the aforementioned results.

Table 4  
The resistance and conductivity of zinc oxide nanoparticles obtained using different electron beam irradiation doses of 0, 15, 20, and 25 KGy.

No. of sample	Slope ( $\Omega$ )	Conductivity (S/m)
0 kGy	$2.67 \times 10^3$	$2.98 \times 10^{-2}$
15 kGy	$1.60 \times 10^3$	$4.97 \times 10^{-2}$
20 kGy	$1.45 \times 10^3$	$5.49 \times 10^{-2}$
25 kGy	$0.64 \times 10^3$	$12.44 \times 10^{-2}$

### 3.4. AC conductivity measurement for irradiated XLPE/ZnO nanocomposites

The variations in AC conductivity as a function of  $\ln(f)$  for irradiated (XLPE/ZnO) nanocomposites with various ZnO contents (i.e., 0, 1, 3, and 5 wt%) after EB irradiation at doses of 0 and 25 kGy are shown in Figure 5a and 5b.

The conductivity of XLPE is also affected by the concentration of ZnO NPs. As shown in Figure 5a, the conductivity of XLPE increased as the ZnO content increased with an irradiation dosage of 0 kGy. The inclusion of filling ZnO NPs in the insulator polymer of the XLPE system can transform it into a good conductor, allowing electrons to delocalize within the entire XLPE chains. Within the XLPE chains, the delocalized electrons move around nearly freely, functioning as conductive charge carriers. XLPE chains can be transformed to pose conductivity by allowing electrons to freely transfer between bonds. The filling procedure using ZnO NPs improves the conductivity of XLPE chains, which are normally nonconductive. ZnO NPs allow electrons to flow to a conductive gap, allowing electrons to move throughout the polymer chain. When electrons transfer along a polymer chain, an electrical current is produced. Figure 5b shows that with increasing radiation doses, the conductivity of the XLPE/ZnO nanocomposite film increases. The experimental AC conductivity data of XLPE/ZnO nanocomposites showed that increasing the irradiation dosage significantly increases the AC conductivity, implying that the irradiation process improves the electrical properties of XLPE/ZnO nanocomposites. The structure of XLPE may be affected by EB irradiation. Depending on the dose, the cross-linked interaction between the XLPE chains changes the physical and chemical characteristics.

### **3.5. Dielectric constant and loss factor for irradiated XLPE/ZnO nanocomposites**

The dielectric constant results of XLPE/ZnO irradiated with EB at 0 and 25 kGy at different ZnO contents (i.e., 0, 1, 3 and 5 wt%) are shown in Figure 6a and 6b. This figure shows that as the frequency increases, the dielectric constant decreases. El-Nahass et al. [41] have observed the same behavior. Note that after frequencies of 125 Hz, the permittivity of the blank XLPE/ZnO nanocomposite sample was frequency-independent. This is because at low frequencies, charge carriers respond quicker to an externally applied electric field, resulting in a higher  $\epsilon'$  value. Moreover, charge carriers at high frequencies could not keep up with the fast changes in the applied electric field, resulting in low  $\epsilon'$  values. The reduction in the dielectric constant as the frequency of the applied field increases might be explained by several types of polarization (i.e., ionic, orientation, and electronic). Ionic polarization occurs when a material is exposed to an electric field, where positive ions move away from negative ions. This polarization intervenes for frequencies smaller than terahertz. Orientation polarization occurs in frequencies ranging between 100 Hz and 450 Hz and is linked to the material structure. The permanent dipoles of the molecules are oriented toward the direction of the applied field in the presence of an applied field. Electronic polarization occurs because the electron cloud of an atom is displaced from its nucleus and all the electrons around it. This type of polarization occurs in a matter of seconds and is sensitive to frequencies well beyond those of visible light ( $10^{15}$  Hz). Orientation polarization is popular because it takes longer than other polarizations. As a result,  $\epsilon'$  decreases until it approaches a constant value at a higher frequency, which corresponds to interfacial polarization. It has a greater dielectric constant than many other aromatic

organic polymers, making it a suitable semiconductor material [42]. In contrast, with the irradiated XLPE/ZnO nanocomposite, the real part of permittivity rose substantially. This is because irradiation contributes to greater allowable charge transfers between molecules in case of a cross-linked structure. It could be predicted that cross-linking at a dosage of 25 kGy results in ZnO NP interconnections and partial polarity elevated by generated radical defects caused by irradiation of materials in the air environment [43]. Due to partial interconnections between ZnO NPs at filler concentrations more than 5 wt%, an increase in the real portion of permittivity at a raised ZnO content affects the dielectric behavior. Figures 6a and 6b shows the effects of EB irradiation and the filler content on AC conductivity. As predicted, the concentration of the conductive filler rose, increasing the irradiated XLPE/ZnO nanocomposite samples. The electrical conductivity of irradiated XLPE/ZnO nanocomposites increased by 24 orders of magnitude at the highest ZnO nanofiller content (the value of permittivity was 135 for non-irradiated XLPE/ZnO nanocomposites with 5 wt% ZnO content (3300), indicating that the percolation threshold had been reached due to the development of a network of the conductive filler).

Figure 7 shows the variations in dielectric loss  $\epsilon''$  with frequency for irradiated XLPE/ZnO nanocomposites at different ZnO contents (i.e., 0, 1, 3, and 5 wt%) upon EB irradiation at 0 and 25 kGy. The dielectric loss factor  $\epsilon''$  of non-irradiated and irradiated XLPE/ZnO nanocomposites. It is because when the frequency rises, the dipolar molecules in the XLPE polymer can respond to the rising rates of the applied field. Interfacial polarization causes the observed increase in dielectric loss  $\epsilon''$  in the low-frequency region [44]. The trend is comparable in both non-irradiated and irradiated XLPE/ZnO nanocomposite samples. Figure 7a and 7b shows an increase in  $\epsilon''$  values with increasing EB dosage. This is due to the presence of charge carriers trapped in the polymer's band gap [45].

### **3.6. Simulation and modeling of electric field distribution inside irradiated XLPE/5-ZnO nanocomposites at 25 kGy**

The electric field distribution in MV cables was simulated using COMSOL Multiphysics. The distribution of electric fields inside XLPE-marked cables is shown in Figure 8. The distribution of electric fields inside XLPE-marked cables was nonuniform at 1-mm arc length (Figure 8). The electric field distribution for the XLPE/5-ZnO nanocomposite sample started to become uniform and gradually decreased from the inside to the outside (Figure 9). This is because ZnO NP-filled XLPE maintained a uniform electrical field and reduced electrostatic stress. Figures 10 and 11 shows the distribution of electric potential in XLPE-marked cables and XLPE/5-ZnO nanocomposite samples, without changes in the behavior curve. For two samples, the electric potential distribution gradually decreased from 24,000 V to 0 V.

## **5. Conclusion**

The maximum uniform electric field was found in the middle of the XLPE/5-ZnO 25-kGy film sample, rather than at the top or bottom, according to the results. This might be attributed to a significantly low relative permittivity of the new XLPE/5-ZnO 25-kGy film cable. COMSOL Multiphysics was used to investigate the distribution of the electric field in XLPE/ZnO NP MV cable insulation under the impacts of

the radius and relative permittivity. The ZnO NPs obtained were classified using TEM. The synthesized ZnO NPs were semi-spheres with sizes of 35–55 nm on TEM images. The band gap increased as the oxidation increased from 3.12 eV to 3.3 eV. The DC conductivity increased as the EB irradiation increased from  $2.98 \times 10^{-2}$  S/m to  $12.44 \times 10^{-2}$  S/m. At low frequencies approaching 120 Hz, the dielectric constant  $\epsilon'$  and dielectric loss  $\epsilon''$  of non-irradiated and irradiated XLPE/ZnO nanocomposite samples were high, and their values increased after the EB irradiation process. The AC conductivity of the polymer under study increased as the frequency and EB irradiation increased. The ZnO NP-filled XLPE maintained a uniform electrical field distribution and decreased electrostatic stress. The optimum AC/DC conductivity (AC:  $1 \times 10^{-4}$  S/m and DC:  $12.44 \times 10^{-2}$  S/m) in the minimum relative permittivity (2.24) was achieved for XLPE/5-ZnO with a ZnO NP content of 5 wt% irradiated at 25 kGy. COMSOL Multiphysics was used to simulate the electric field distribution within the MV cable of XLPE/5-ZnO irradiated at 25 kGy. Therefore, it is recommended that the XLPE market should be modified by adding ZnO NPs (5 wt%) and EB irradiated at 25 kGy. In producing scientific goods, the synthesis of ZnO NPs is of considerable importance.

## References

1. D. Ponnamma et al., Synthesis, optimization and applications of ZnO/polymer nanocomposites. *Mater. Sci. Engineering: C* **98**, 1210–1240 (2019)
2. A. Janotti, C.G. Van de Walle, Fundamentals of zinc oxide as a semiconductor. *Rep. Prog. Phys.* **72**(12), 126501 (2009)
3. A. Hezam et al., Direct Z-scheme Cs<sub>2</sub>O–Bi<sub>2</sub>O<sub>3</sub>–ZnO heterostructures for photocatalytic overall water splitting. *J. Mater. Chem. A* **6**(43), 21379–21388 (2018)
4. S.K. Patil, S.S. Shinde, K.Y. Rajpure, Physical properties of spray deposited Ni-doped zinc oxide thin films. *Ceram. Int.* **39**(4), 3901–3907 (2013)
5. S. Yilmaz et al., Defect-induced room temperature ferromagnetism in B-doped ZnO. *Ceram. Int.* **39**(4), 4609–4617 (2013)
6. S. Suwanboon et al., Physical and chemical properties of multifunctional ZnO nanostructures prepared by precipitation and hydrothermal methods. *Ceram. Int.* **40**(1), 975–983 (2014)
7. S. Labuayai, V. Promarak, S. Maensiri, Synthesis and optical properties of nanocrystalline ZnO powders prepared by a direct thermal decomposition route. *Appl. Phys. A* **94**(4), 755–761 (2009)
8. S.C. Ko et al., Micromachined piezoelectric membrane acoustic device. **103**(1-2), 130–134 (2003)
9. D. Zaouk et al., Piezoelectric zinc oxide by electrostatic spray pyrolysis. **37**(11), 1276–1279 (2006)
10. L. Panchakarla, A. Govindaraj, S. C.J.J.o.C, Rao, Formation of ZnO nanoparticles by the reaction of zinc metal with aliphatic alcohols. **18**(3), 660–670 (2007)
11. H. Hayashi et al., *Bright blue phosphors in ZnO–WO<sub>3</sub> binary system discovered through combinatorial methodology*. 2003. **82**(9): p. 1365–1367

12. H.T. Ng et al., *Optical properties of single-crystalline ZnO nanowires on m-sapphire*. 2003. 82(13): p. 2023–2025
13. P.X. Gao et al., *Conversion of zinc oxide nanobelts into superlattice-structured nanohelices*. 2005. 309(5741): p. 1700–1704
14. X. Cheng et al., *ZnO nanoparticulate thin film: preparation, characterization and gas-sensing property*. 2004. **102**(2): p. 248-252
15. E. Topoglidis et al., *Immobilisation and bioelectrochemistry of proteins on nanoporous TiO<sub>2</sub> and ZnO films*. 2001. 517(1-2): p. 20–27
16. Y. Hames et al., *Electrochemically grown ZnO nanorods for hybrid solar cell applications*. 2010. 84(3): p. 426–431
17. W. Jun et al., *Preparation of ZnO-glass varistor from tetrapod ZnO nanopowders*. 2002. 95(2): p. 157–161
18. P. Sharma, K. Sreenivas, K.J.J.o.AP. Rao, *Anal. Ultrav. photoconductivity ZnO films prepared unbalanced magnetron sputtering* **93**(7), 3963–3970 (2003)
19. P.V. Kamat, R. Huehn, C.B. R.J.T.J.o.P. Nicolaescu, A “sense and shoot”. approach for. photocatalytic degradation of organic contaminants in water **106**(4), 788–794 (2002)
20. G. Mazitova et al., *Synthesis and Properties of Zinc Oxide Nanoparticles: Advances and Prospects*. 2019. **9**(2): p. 127-152
21. M.K. Lima et al., *Co-doped ZnO nanoparticles synthesized by an adapted sol–gel method: effects on the structural, optical, photocatalytic and antibacterial properties*. 2014. **72**(2): p. 301-309
22. Y. Caglar et al., *Effect of channel thickness on the field effect mobility of ZnO-TFT fabricated by sol gel process*. 2015. 621: p. 189–193
23. M.S. Tokumoto et al., *Catalysis and temperature dependence on the formation of ZnO nanoparticles and of zinc acetate derivatives prepared by the sol– gel route*. 2003. 107(2): p. 568–574
24. M. Singhai et al., *Synthesis of ZnO nanoparticles for varistor application using Zn-substituted aerosol OT microemulsion*. 1997. 32(2): p. 239–247
25. F. Rataboul et al., *Synthesis and characterization of monodisperse zinc and zinc oxide nanoparticles from the organometallic precursor [Zn (C<sub>6</sub>H<sub>11</sub>)<sub>2</sub>]*. 2002. **643**: p. 307-312
26. K. Okuyama, and I.W.J.C.e.s. Lenggoro. Preparation of nanoparticles via spray route. **58**(3-6), 537–547 (2003)
27. A.B. Moghaddam et al., *Synthesis of ZnO nanoparticles and electrodeposition of polypyrrole/ZnO nanocomposite film*. 2009. 4(2): p. 247–257
28. Y.-L. Wei, P.-C.J.J.o.P. Chang, C.o. Solids, Characteristics of nano zinc oxide synthesized under ultrasonic condition. **69**(2-3), 688–692 (2008)
29. X.-L. Hu et al., *Sonochemical and microwave-assisted synthesis of linked single-crystalline ZnO rods*. 2004. 88(2-3): p. 421–426

30. J.J. Wu, S.C.J.A.m. Liu, Low-temperature growth of well-aligned ZnO nanorods by chemical vapor deposition. **14**(3), 215–218 (2002)
31. H.-J. Zhai et al., *Effects of ammonia and cetyltrimethylammonium bromide (CTAB) on morphologies of ZnO nano-and micromaterials under solvothermal process*. 2008. **112**(3): p. 1024-1028
32. M. Bitenc, M. Marinšek, and Z.C.J.J.o.t.E.C.S. Orel, *Preparation and characterization of zinc hydroxide carbonate and porous zinc oxide particles*. 2008. 28(15): p. 2915–2921
33. S. Raghu et al., Effect of electron beam irradiation on polymer electrolytes: Change in morphology, crystallinity, dielectric constant and AC conductivity with dose. *Radiat. Phys. Chem.* **98**, 124–131 (2014)
34. J. Wei, L. Zhu, *Intrinsic polymer dielectrics for high energy density and low loss electric energy storage*. *Progress in Polymer Science*, 2020: p. 101254
35. S. Raghu et al., Electron. beam and gamma ray irradiated polymer electrolyte films: Dielectric properties **9**(2), 117–124 (2016)
36. A. Sharshir et al., *Simulating the electric field distribution in medium-voltage cables of cross-linked polyethylene/Cu nanocomposites irradiated by E-beam with reference to the XLPE market*. 2021: p. 1–12
37. C. Kim et al., *Investigation on dielectric breakdown behavior of thermally aged cross-linked polyethylene cable insulation*. 2019. **80**: p. 106045
38. W. Lei et al., Are nano-composites really better DC insulators? A study using silica nanoparticles in XLPE. *IEEE Trans. Dielectr. Electr. Insul.* **24**(4), 2268–2270 (2017)
39. S. Moniri et al., Synthesis and optical characterization of copper nanoparticles prepared by laser ablation. *Bull. Mater. Sci.* **40**(1), 37–43 (2017)
40. S. Fayek et al., *Study of  $\gamma$ -rays Changes of the ZnO Thin Film Structural and Optical Properties*. 2018. 51(1): p. 204–214
41. M. El-Nahass et al., *AC conductivity and dielectric characterization of synthesized pN, N dimethylaminobenzylidenemalononitrile (DBM) organic dye*. 2013. 91: p. 14–19
42. H. Bouaamlat et al., *Dielectric properties, AC conductivity, and electric modulus analysis of bulk ethylcarbazole-terphenyl*. 2020. **2020**
43. E. Suljovrujic, Dielectric study of post-irradiation effects in gamma-irradiated polyethylenes. *Radiat. Phys. Chem.* **79**(7), 751–757 (2010)
44. S. Rajendran, M. Sivakumar, R. Subadevi, Investigations on the effect of various plasticizers in PVA–PMMA solid polymer blend electrolytes. *Mater. Lett.* **58**(5), 641–649 (2004)
45. K. Velitchkova, K. Krezhov, S. Balabanov, Temperature dependence of surface DC electrical conductivity of carbon-implanted polymers modified by gamma irradiation. *Vacuum* **58**(2-3), 531–535 (2000)

## Figures

Figure 1

(a) X-ray diffraction spectra and (b) Fourier transform infrared spectroscopy spectra were obtained using the three preparation methods. (c) Transmission electron microscopy images of zinc oxide nanoparticles obtained using the oxalic acid method.

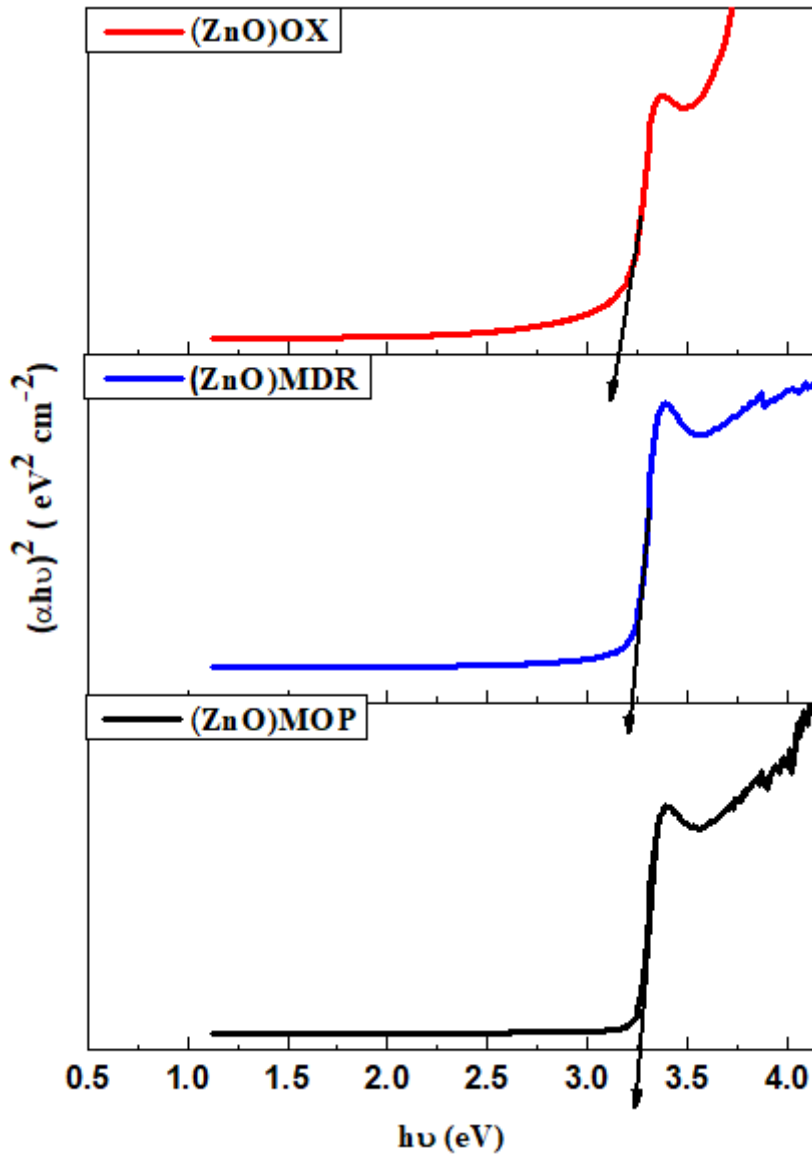


Figure 2

The calculation of the band gap energy of zinc oxide nanoparticles.

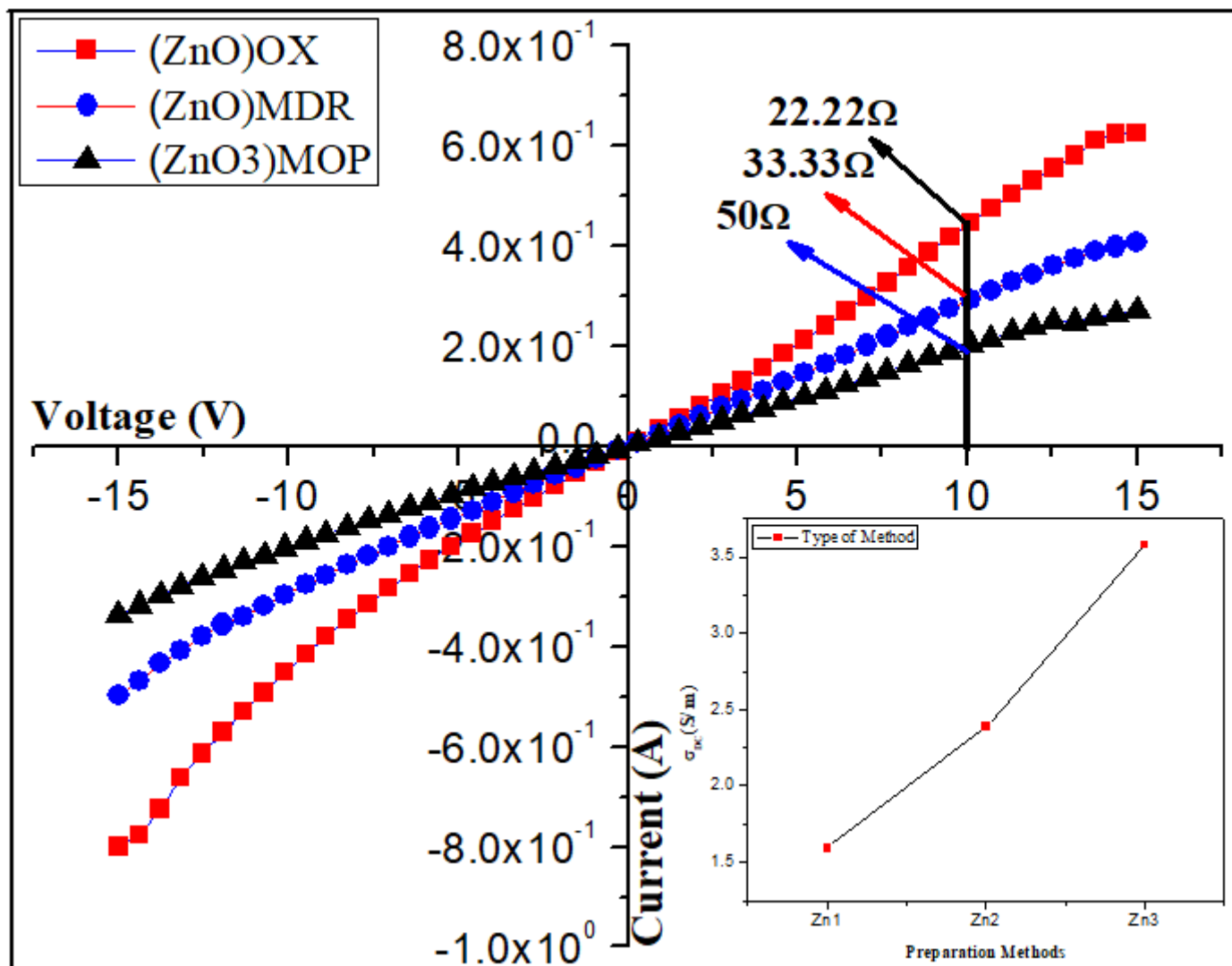
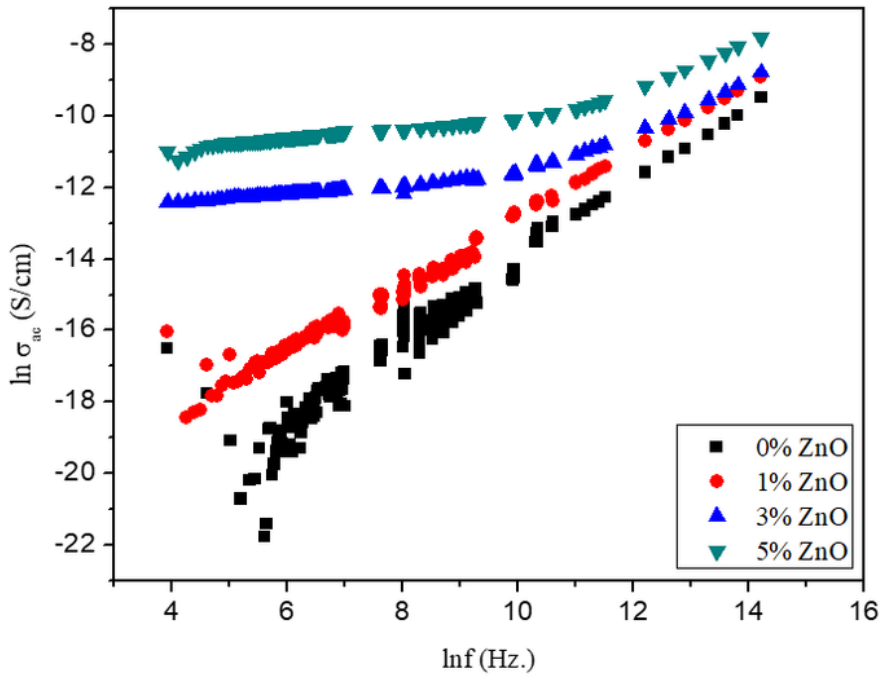
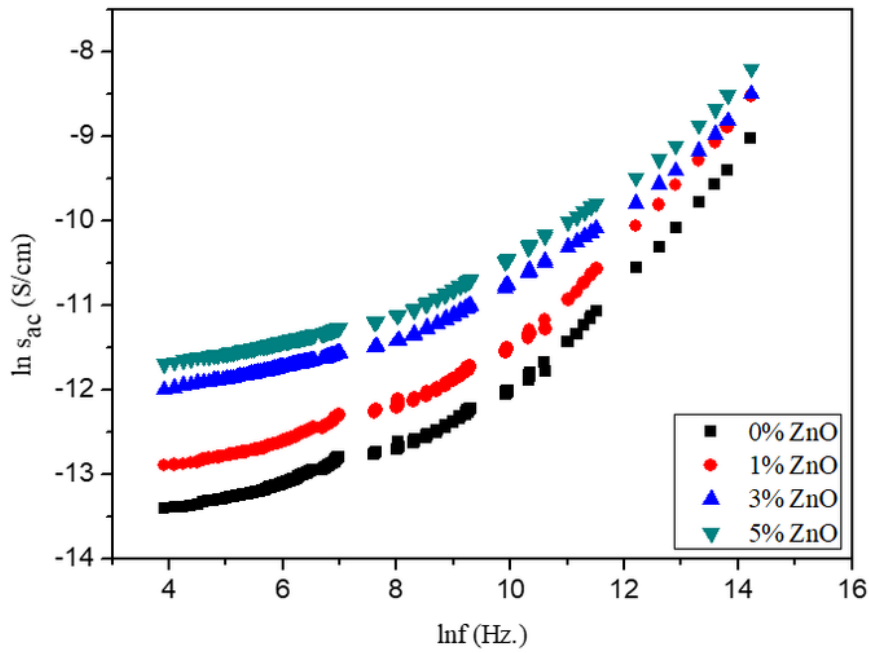


Figure 3

I-V curve of (ZnONPS) . The inner curve shows the electrical conductivity of ZnO NPs obtained using the three preparation methods.



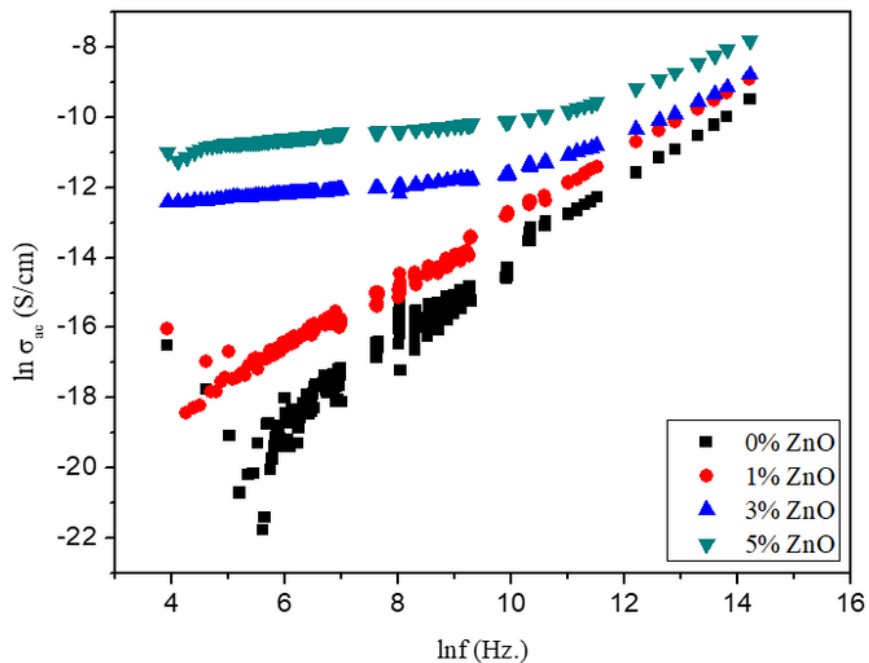
(a)



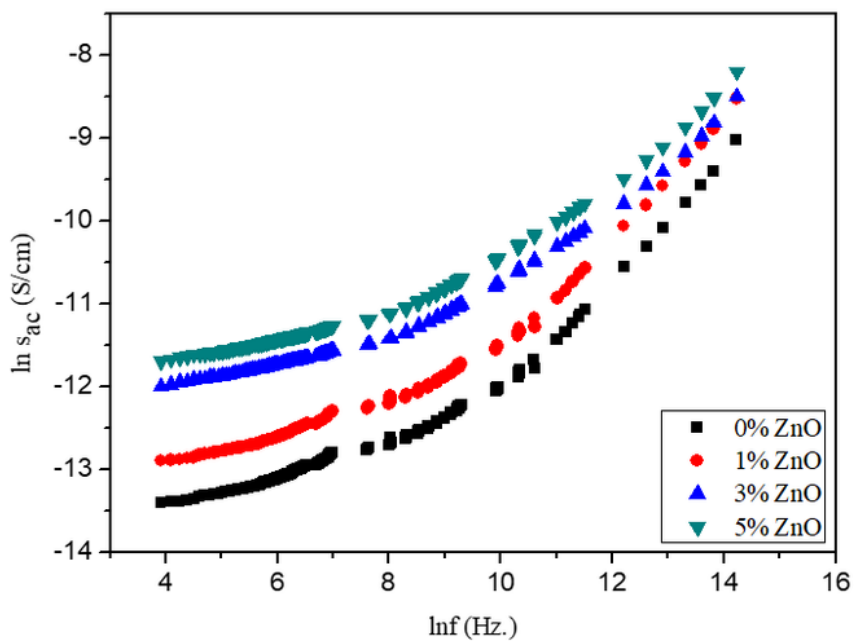
(b)

**Figure 4**

I–V curve of (XLPE/5-ZnO). The inner curve shows the electrical conductivity of zinc oxide (ZnO) nanoparticles (NPs) obtained at different electron beam doses (i.e., 0, 15, 20, and 25 kGy).



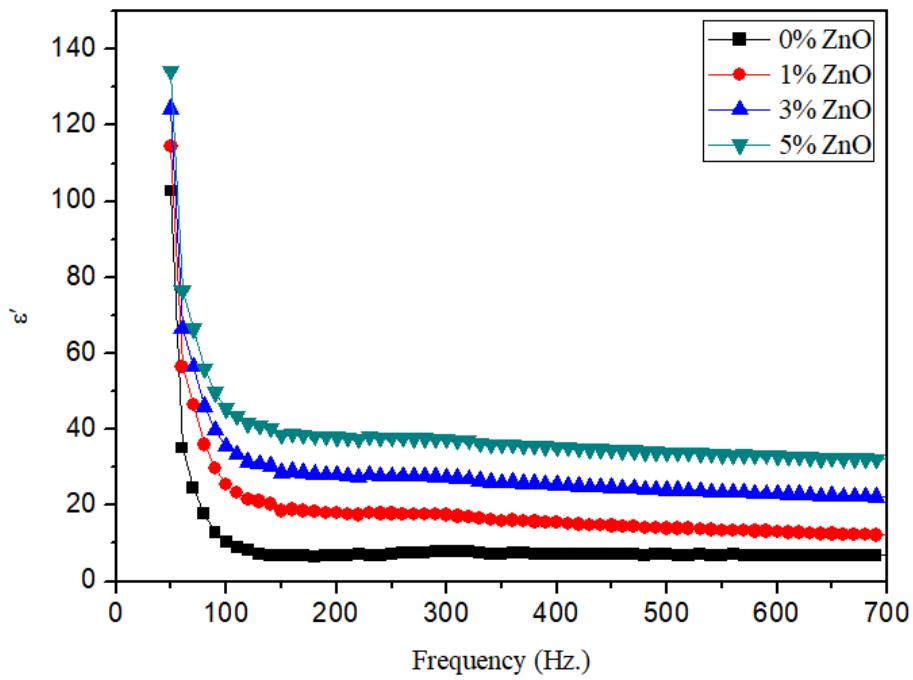
(a)



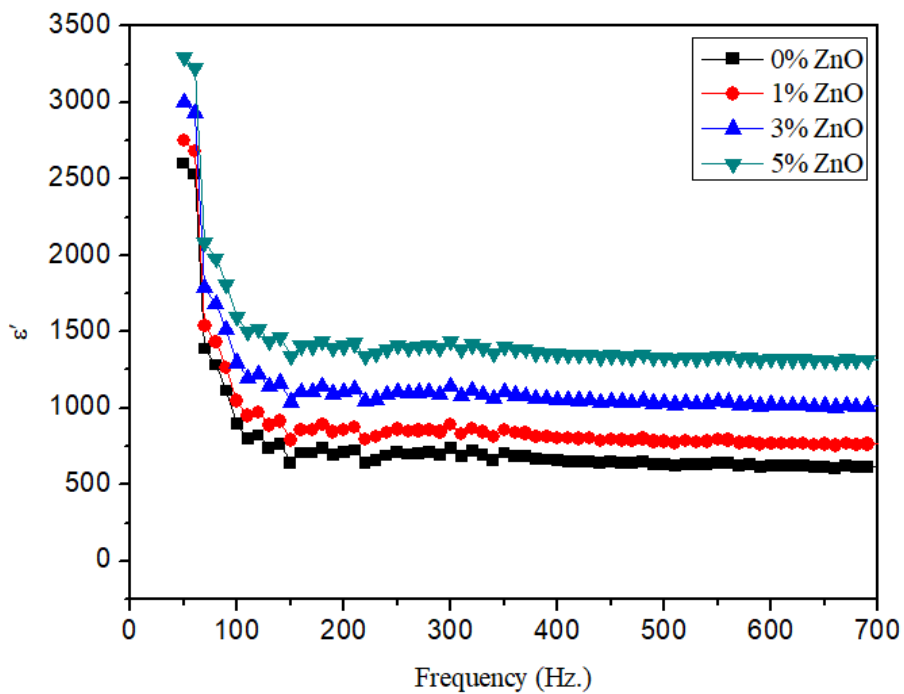
(b)

**Figure 5**

Frequency dependence of alternating current (AC) conductivity for zinc oxide nanoparticle-filled (i.e., 0, 1%, 3%, and 5%) cross-linked polyethylene at 0 kGy (a) and 25 kGy (b). The AC conductivity increases as the frequency increases due to the effects of the electron beam dose (25 kGy).



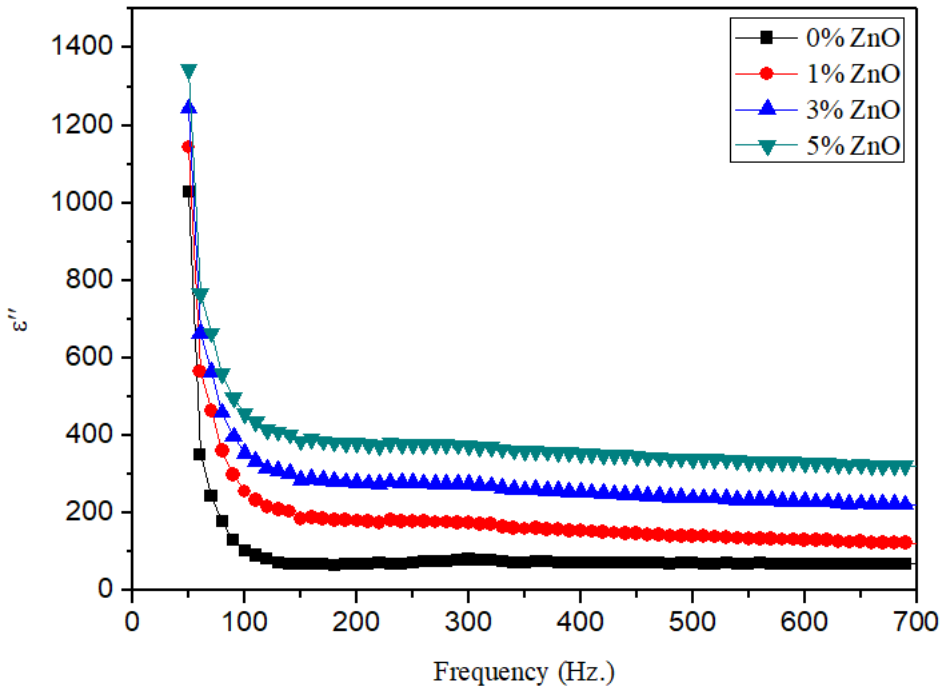
(a)



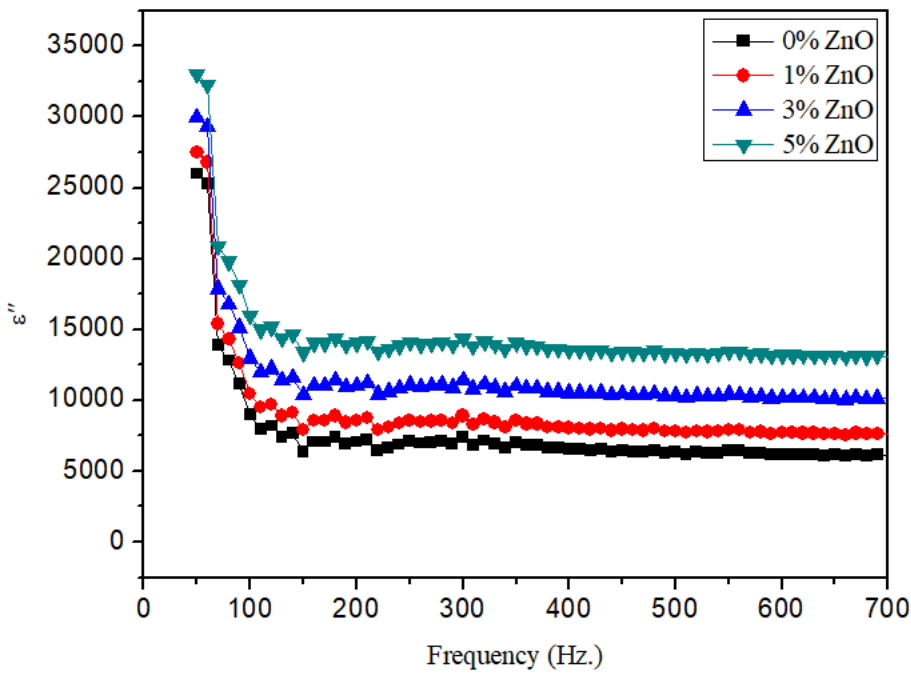
(b)

**Figure 6**

Frequency dependence of dielectric constant  $\epsilon'$  for zinc oxide nanoparticle-filled (i.e., 0, 1%, 3%, and 5%) cross-linked polyethylene irradiated at 0 and 25 kGy.



(a)



(b)

**Figure 7**

Frequency dependence of dielectric loss  $\epsilon''$  for zinc oxide nanoparticle-filled (i.e., 0, 1%, 3%, and 5%) irradiated cross-linked polyethylene at 0 kGy (a) and 25 kGy (b).

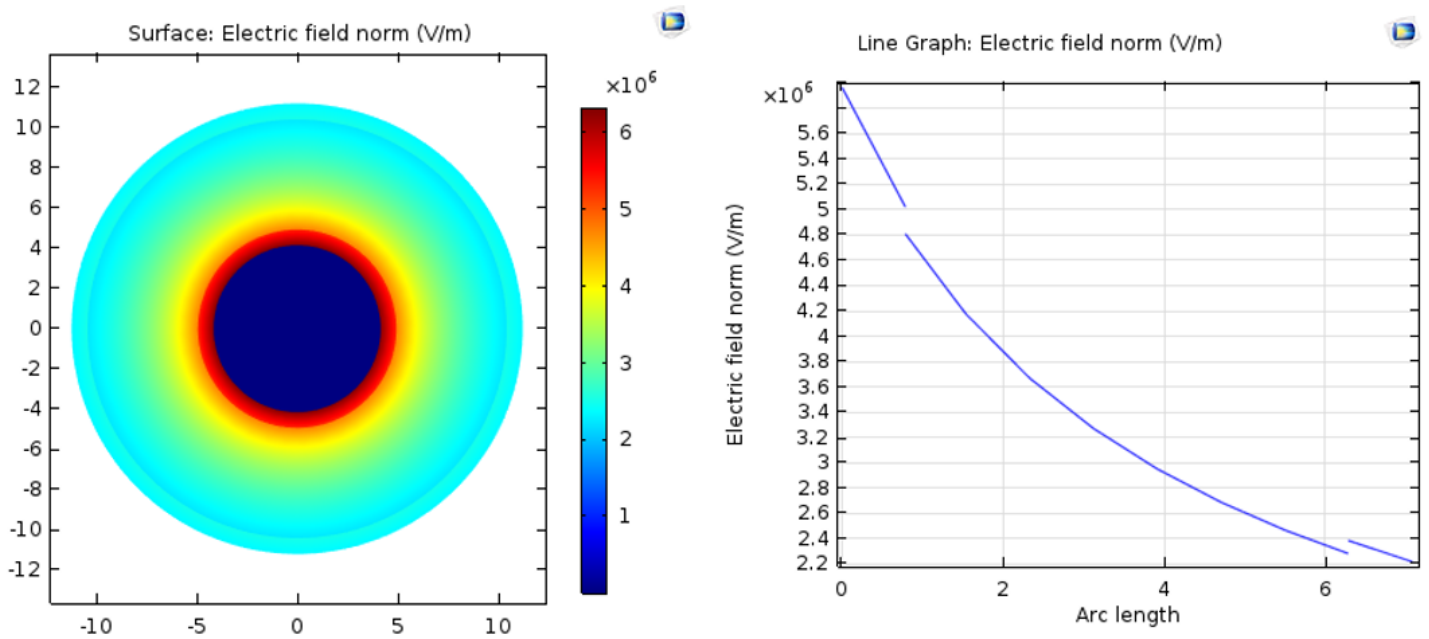


**Figure 8**

Electric field distribution in medium-voltage cross-linked polyethylene-marked cables without zinc oxide filling.

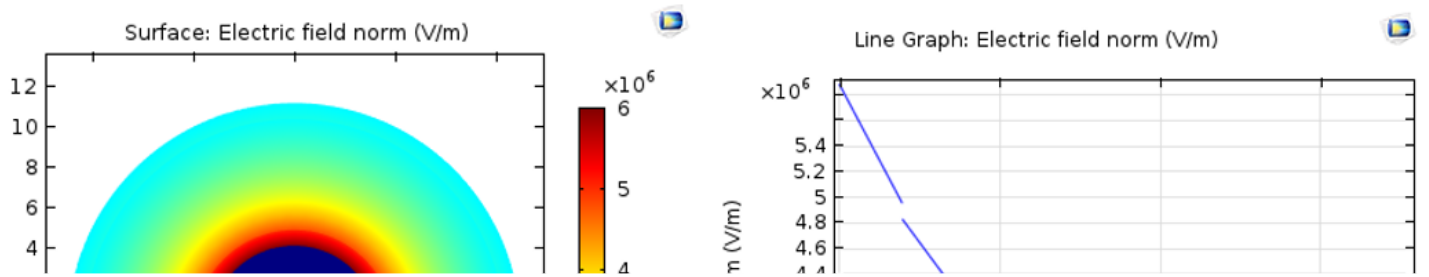


**Figure 9**

Electric field distribution in medium-voltage cables with zinc oxide (ZnO) filling of polyethylene/5-ZnO irradiated at 25 kGy.

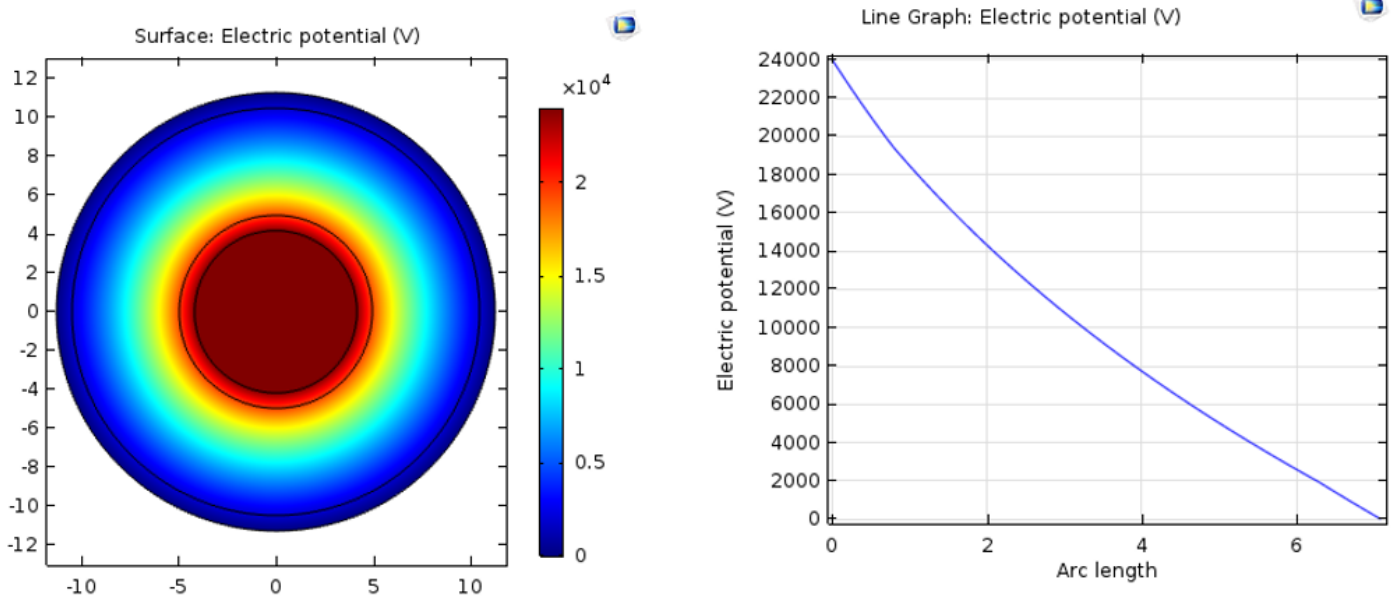


**Figure 10**

Electric potential distribution in medium-voltage cross-linked polyethylene-marked cables without zinc oxide filling.

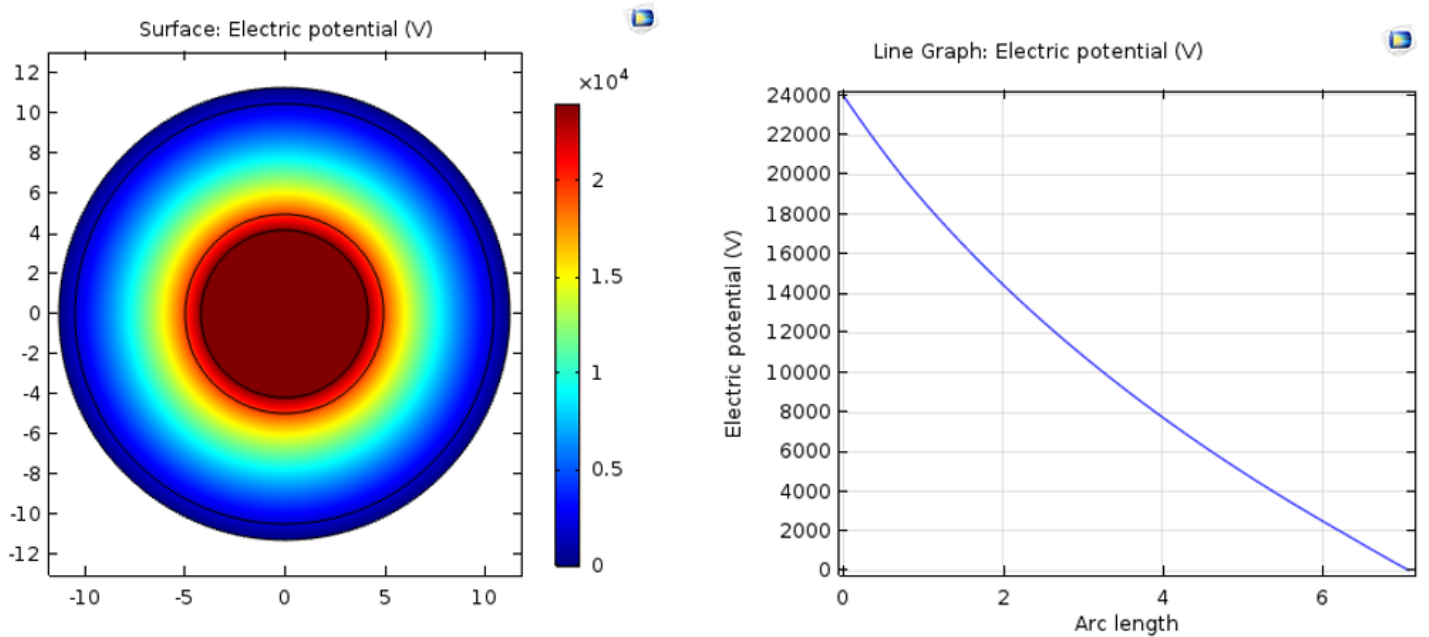


**Figure 11**

Electric potential distribution in medium-voltage cables with zinc oxide (ZnO) filling of cross-linked polyethylene/5-ZnO irradiated at 25 kGy.